

# **Turbulence Model Predictions of Strongly Curved Flow in a U-Duct**

C. L. Rumsey, T. B. Gatski, J. H. Morrison

Reprinted from

**AIAA Journal**

Volume 38, Number 8, Pages 1394–1402



*A publication of the*  
American Institute of Aeronautics and Astronautics, Inc.  
1801 Alexander Bell Drive, Suite 500  
Reston, VA 20191-4344



# Turbulence Model Predictions of Strongly Curved Flow in a U-Duct

Christopher L. Rumsey,\* Thomas B. Gatski,<sup>†</sup> and Joseph H. Morrison<sup>‡</sup>  
NASA Langley Research Center, Hampton, Virginia 23681-2199

The ability of three types of turbulence models to accurately predict the effects of curvature on the flow in a U-duct is studied. An explicit algebraic stress model performs slightly better than one- or two-equation linear eddy viscosity models, although it is necessary to fully account for the variation of the production-to-dissipation-rate ratio in the algebraic stress model formulation. In their original formulations, none of these turbulence models fully captures the suppressed turbulence near the convex wall, whereas a full Reynolds stress model does. Some of the underlying assumptions used in the development of algebraic stress models are investigated and compared with the computed flowfield from the full Reynolds stress model. Through this analysis, the assumption of Reynolds stress anisotropy equilibrium used in the algebraic stress model formulation is found to be incorrect in regions of strong curvature. By the accounting for the local variation of the principal axes of the strain rate tensor, the explicit algebraic stress model correctly predicts the suppressed turbulence in the outer part of the boundary layer near the convex wall.

## I. Introduction

MANY flowfields being calculated by computational fluid dynamics (CFD) codes are so complex that it can be difficult to determine the source of error in comparison with experiment. For example, the flow over a multielement airfoil contains a wide variety of challenging physical processes, including confluent boundary layers, wakes in adverse pressure gradient, separated flows, possible unsteady flow, possible shock-/boundary-layer interactions, and significant streamline curvature. Current state-of-the-art CFD codes do not predict certain aspects of the physics of multielement airfoil flows accurately enough for design studies.<sup>1</sup> Turbulence models are often assigned the blame, but due to the complexities of the multielement flowfield it is not certain why the models are deficient. (In fact, many other factors may contribute, such as improper transition modeling or lack of three-dimensional effects in two-dimensional computations.) For turbulence model developers to determine how to improve their models, it is important to isolate and quantify the various effects of significance to the problem of interest, and to evaluate turbulence models in such flows.

For example, the flow off the main element on a multi-element airfoil configuration can turn as much as 30–40 deg as it passes over the flap. It is possible that such turning (convex curvature) has an impact on the Reynolds shear stresses in that region, which in turn may affect the mean flow over the flap. Comparisons of computed Reynolds shear stresses with experimentally measured values in the flap region indicate that some discrepancies exist.<sup>2</sup> Currently, it is uncertain whether the disagreement is due to the turbulence model itself, or whether other factors are to blame. In particular, note that the  $\delta/R$  parameter (boundary-layer thickness over radius of curvature) that defines the turning of the flow over the flap can be on the order of 0.01–0.1, depending on the particular configuration and whether the main element wake is included in the determination

of  $\delta$ . In general,  $\delta/R < 0.01$  represents very mild curvature, whereas  $0.1 < \delta/R < 1$  represents moderate to strong curvature.<sup>3</sup>

Monson and Seegmiller<sup>4</sup> and Monson et al.<sup>5</sup> performed a nominally two-dimensional experiment on flow through a U-duct (with aspect ratio 10 and side-wall suction upstream of the bend) and evaluated the abilities of several turbulence models to predict both the mean flow (velocity profiles, skin friction, and surface pressure) and turbulence quantities (turbulent kinetic energy and Reynolds shear stress). The curvature was strong in this setup, with  $\delta/R$  approximately 0.5 around the inner wall. The U-duct is representative of many internal flows of engineering interest, such as flow in the turnaround duct in the Space Shuttle main engine powerhead.

Although the Monson and Seegmiller<sup>4</sup> data contains separated flow on the inner wall beyond the bend and, therefore, is unlikely to retain its two-dimensional character at and beyond this region, the flow in the bend leading up to separation is well defined and nominally two-dimensional. Therefore, it is an ideal test case to investigate the effect of strong convex curvature and to evaluate the ability of existing turbulence models to predict the physics of curvature. Sandborn and Marcy<sup>6</sup> investigated a U-duct configuration in a water tunnel and reported similar results to Monson and Seegmiller's data in the bend upstream of separation. Many other curved duct flow experiments have been performed (e.g., Refs. 7–11), but most either do not explicitly define the outer wall geometry or else have lower aspect ratios (and hence more significant three-dimensional effects). These ambiguities limit the usefulness of such studies for turbulence model validation.

In Ref. 5 seven isotropic eddy viscosity turbulence models (one algebraic and six  $K-\epsilon$  models) evaluated against the Monson and Seegmiller<sup>4</sup> data met with varying degrees of success regarding prediction of skin friction, but none of them consistently predicted the measured mean velocities downstream of the turn or the turbulence quantities in or downstream of the turn. Luo and Lakshminarayana<sup>12</sup> computed the same configuration using four levels of turbulence model approximations: a linear eddy viscosity  $K-\epsilon$  model, a nonlinear (NL)  $K-\epsilon$  model, an implicit algebraic Reynolds stress model (ARSM), and a full Reynolds stress model (RSM). All models were linked to a near-wall one-equation model near  $y^+ = 70$ . The eddy viscosity model predicted very high Reynolds shear stress over the convex wall and a too-small extent of separation. The other models were better, but only the RSM predicted nearly complete suppression of Reynolds shear stress over the convex wall as seen in the experiment.

Many other computations of turbulent curved flows for similar configurations have been done, only a few of which are mentioned here. Rodi and Scheuerer<sup>13</sup> examined three extensions to the  $K-\epsilon$  model, including an algebraic stress model without

Presented as Paper 99-0157 at the AIAA 37th Aerospace Sciences Meeting, Reno, NV, 11–14 January 1999; received 10 May 1999; revision received 28 December 1999; accepted for publication 5 January 2000. Copyright © 2000 by the American Institute of Aeronautics and Astronautics, Inc. No copyright is asserted in the United States under Title 17, U.S. Code. The U.S. Government has a royalty-free license to exercise all rights under the copyright claimed herein for Governmental purposes. All other rights are reserved by the copyright owner.

\*Senior Research Scientist, Aerodynamics, Aerothermodynamics, and Acoustics Competency, Associate Fellow AIAA.

<sup>†</sup>Senior Research Scientist, Aerodynamics, Aerothermodynamics, and Acoustics Competency.

<sup>‡</sup>Senior Research Scientist, Aerodynamics, Aerothermodynamics, and Acoustics Competency, Senior Member AIAA.

curvature-specific empiricism. They found that this algebraic stress model gives the best overall agreement in the curved part of the flow. Luo and Lakshminarayana<sup>14</sup> found that, although an RSM can successfully capture the large damping of turbulence near a convex wall, it underpredicts the enhancement of turbulence near a concave wall; to capture the amplification, they concluded that the standard  $\varepsilon$  equation needs to be modified. Iacovides et al.<sup>15</sup> evaluated an algebraic stress model and Shima<sup>16</sup> evaluated an RSM; both methods were found to be superior to linear two-equation models for curved flows.

Rumsey et al.<sup>17</sup> evaluated several turbulence models for multi-element airfoil flows. Two of these models, the one-equation Spalart–Allmaras<sup>18</sup> (S–A) and the two-equation Menter<sup>19</sup> shear-stress transport (SST)  $K$ – $\omega$ , are isotropic eddy viscosity models that are used extensively in production CFD codes. The third model is the explicit algebraic stress model (EASM) of Gatski and Speziale.<sup>20</sup> For the flowfields explored by Rumsey et al.,<sup>17</sup> all three models showed minor differences from each other, but they also each showed gross deficiencies in comparison with experiment, attributed primarily to poor transition modeling over the slat. Because of the gross deficiencies, it proved to be impossible to distinguish among the turbulence models themselves or recommend areas for turbulence model improvement.

In the current work, we apply the same three turbulence models to flow in the two-dimensional U-duct, and investigate their ability to model the physics due to strong curvature. We focus our attention primarily on the inner (convex) wall upstream of separation, where the experimental data is nominally two dimensional. Recent advances in the explicit algebraic stress formulation<sup>21–24</sup> are explored in relation to this flow. Then, the assumption of Reynolds stress anisotropy equilibrium used to derive the EASM is evaluated and subsequently modified to account for curvature in that model. Note that we do not seek to develop an ad hoc curvature correction for the EASM, but rather we seek to evaluate and improve the assumptions made in its derivation directly from the RSM in a mathematically rigorous fashion. Both the U-duct and a second experiment of Smits et al.<sup>25</sup> are used for validation of the EASM curvature correction.

Through this study, flowfield curvature, one of the component physical processes of possible importance in the flow over complex configurations, is explored. Separate on-going work focuses on other aspects, including wake development in an adverse pressure gradient and transition. By exploring the component pieces (that is, unit problems), we hope to address specific deficiencies in existing turbulence models and develop better turbulence models in the future.

## II. Description of the Codes

The computer code CFL3D<sup>26</sup> solves the three-dimensional, time-dependent, Reynolds averaged Navier–Stokes equations with an upwind finite volume formulation. It can solve flows over multiple-zone grids that are connected in a one-to-one, patched, or overset manner and can employ grid sequencing, multigrid, and local time stepping when accelerating convergence to steady state. Upwind-biased spatial differencing is used for the inviscid terms, and flux limiting is used to obtain smooth solutions in the vicinity of shock waves, when present. Viscous terms are centrally differenced, and cross-diffusion terms (which only come into play on nonorthogonal grids) are neglected.

The CFL3D code is advanced in time with an implicit approximate factorization method. The implicit derivatives are written as spatially first-order accurate, which results in block tridiagonal inversions for each sweep. However, for solutions that utilize flux-difference splitting, the block tridiagonal inversions are further simplified using a diagonal algorithm with a spectral radius scaling of the viscous terms.

The turbulence models are solved uncoupled from the mean flow equations. Descriptions of the S–A and SST turbulence models can be found in their respective references,<sup>18,19</sup> and a detailed description of the EASM is given in the next section.

The computer code ISAAC<sup>27</sup> is also employed in one portion of the current study. The ISAAC code is functionally very similar to the CFL3D code, but it possesses higher-order turbulence models, including RSMs. The turbulence models in ISAAC are solved fully coupled with the mean flow equations.

## III. Algebraic Stress Model Methodology

The application of algebraic stress models (ASMs) to a variety of flow problems has become commonplace. With this increase in use has also come a variety of formulations. These formulations differ in the number of basis terms used in the tensor representation and in the particular means by which the ASM is implemented. The ASM used in this study is based on the model originally developed by Gatski and Speziale,<sup>20</sup> but extended and implemented based on a formulation developed by Jongen and Gatski.<sup>28</sup> The reader is referred to these earlier studies for additional background.

### A. General ASM

The common starting point for the development of ASMs is the modeled transport equation for the Reynolds stress tensor  $\tau_{ij}$  given by

$$\begin{aligned} \frac{1}{2K} \left[ \frac{D\tau_{ij}}{Dt} - \frac{\tau_{ij}}{K} \frac{DK}{Dt} \right] - \frac{1}{2K} \left[ \mathcal{D}_{ij} - \frac{\tau_{ij}}{2K} \mathcal{D}_{nn} \right] \\ = -\frac{1}{a_4} b_{ij} - a_3 \left( b_{ik} S_{kj} + S_{ik} b_{kj} - \frac{2}{3} b_{kl} S_{ik} \delta_{ij} \right) \\ + a_2 (b_{ik} W_{kj} - W_{ik} b_{kj}) - R_{ij} \\ = -\frac{1}{a_4} \mathbf{b} - a_3 \left( \mathbf{bS} + \mathbf{Sb} - \frac{2}{3} \{\mathbf{bS}\} \mathbf{I} \right) + a_2 (\mathbf{bW} - \mathbf{Wb}) - \mathbf{R} \end{aligned} \quad (1)$$

where  $K = \frac{1}{2} \tau_{nn}$  is the turbulence kinetic energy,  $\mathcal{D}_{ij}$  is the turbulent transport and viscous diffusion tensor, and  $\{\mathbf{bS}\} = b_{ij} S_{ji}$  is the trace. The tensor  $\mathbf{R} = a_1 \mathbf{S}$  when a linear pressure–strain correlation model is assumed as well as an isotropic dissipation rate  $\varepsilon$ , but  $\mathbf{R}$  can in general be any symmetric traceless tensor.<sup>28</sup> The kinematic strain rate and rotation rate tensors,  $S_{ij}$  and  $W_{ij}$ , respectively, are

$$S_{ij} = \frac{1}{2} \left( \frac{\partial u_i}{\partial x_j} + \frac{\partial u_j}{\partial x_i} \right), \quad W_{ij} = \frac{1}{2} \left( \frac{\partial u_i}{\partial x_j} - \frac{\partial u_j}{\partial x_i} \right)$$

and the Reynolds stress anisotropy tensor is defined as

$$b_{ij} = \tau_{ij}/2K - \frac{1}{3} \delta_{ij} \quad (2)$$

The coefficients  $a_i$  are directly related to the pressure–strain correlation model used in closing the stress transport equation. This study uses the Speziale–Sarkar–Gatski (SSG) pressure–strain model,<sup>29</sup> which yields

$$\begin{aligned} a_1 &= \frac{1}{2} \left( \frac{4}{3} - C_2 \right), & a_2 &= \frac{1}{2} (2 - C_4) \\ a_3 &= \frac{1}{2} (2 - C_3), & a_4 &= g\tau, & \tau &= K/\varepsilon \end{aligned} \quad (3)$$

$$g = \left[ (C_1^1/2 + 1)(\mathcal{P}/\varepsilon) + \frac{1}{2} C_1^0 - 1 \right]^{-1} = [\gamma_0(\mathcal{P}/\varepsilon) + \gamma_1]^{-1} \quad (4)$$

where  $C_1^0 = 3.4$ ,  $C_1^1 = 1.8$ ,  $C_2 = 0.36$ ,  $C_3 = 1.25$ , and  $C_4 = 0.4$ .

An implicit algebraic stress relation is obtained from the modeled transport equation for the Reynolds stresses [Eq. (1)] when the following two assumptions are made:

$$\mathcal{D}_{ij} = (\tau_{ij}/2K) \mathcal{D}_{nn} \quad (5)$$

$$\frac{D\tau_{ij}}{Dt} = \frac{\tau_{ij}}{K} \frac{DK}{Dt} \quad (6)$$

Equation (6) is equivalent to requiring that the turbulence has reached an equilibrium state,  $Db/Dt = 0$ . With these assumptions, the left-hand side of Eq. (1) vanishes, and the equation becomes algebraic:

$$-(1/a_4) \mathbf{b} - a_3 \left( \mathbf{bS} + \mathbf{Sb} - \frac{2}{3} \{\mathbf{bS}\} \mathbf{I} \right) + a_2 (\mathbf{bW} - \mathbf{Wb}) = \mathbf{R} \quad (7)$$

Equation (7) has to be solved for  $\mathbf{b}$  and is an implicit equation. For the case  $\mathbf{R} = a_1 \mathbf{S}$ , an explicit solution of Eq. (7) has been obtained by Gatski and Speziale<sup>20</sup> for two-dimensional mean flows in the form

$$\mathbf{b} = \alpha_1 \mathbf{S} + \alpha_2 (\mathbf{S}\mathbf{W} - \mathbf{W}\mathbf{S}) + \alpha_3 (\mathbf{S}^2 - \frac{1}{3} \{\mathbf{S}^2\} \mathbf{I}) \quad (8)$$

where the  $\alpha_i$  are scalar coefficient functions of the invariants  $\eta^2 (= \{\mathbf{S}^2\})$  and  $\mathcal{R}^2 (= -\{\mathbf{W}^2\}/\{\mathbf{S}^2\})$ . (Here,  $\mathcal{R}^2$  is a nondimensional flow parameter that is very useful for characterizing the flow<sup>23,30</sup>; for example, for a pure shear flow  $\mathcal{R}^2 = 1$ , whereas for a plane strain flow  $\mathcal{R}^2 = 0$ .) A new methodology for identifying the coefficients  $\alpha_i$ , such that Eq. (8) is the solution of the general stress relation Eq. (7), will now be derived.

### B. Explicit Solution

Consider a three-term tensor representation given by

$$\mathbf{b} = \sum_{n=1}^3 \alpha_n \mathbf{T}^{(n)} \quad (9)$$

with the three-term tensor basis  $\mathbf{T}^{(m)}$ :

$$\mathbf{T}^{(1)} = \mathbf{S}, \quad \mathbf{T}^{(2)} = \mathbf{S}\mathbf{W} - \mathbf{W}\mathbf{S}, \quad \mathbf{T}^{(3)} = \mathbf{S}^2 - \frac{1}{3} \{\mathbf{S}^2\} \mathbf{I} \quad (10)$$

As discussed by Jongen and Gatski,<sup>28</sup> higher-term bases ( $N \geq 5$ ) are also possible, but we consider here only the three-term basis, which is exact for two-dimensional flows.

Equation (7) can be solved via the Galerkin method by projecting this algebraic relation onto the tensor basis  $\mathbf{T}^{(m)}$  itself. For this, we form the scalar product of Eq. (7) with each of the tensors  $\mathbf{T}^{(m)}$  ( $m = 1, 2, 3$ ). This leads to the following system of equations:

$$\sum_{n=1}^3 \alpha_n \left[ -\frac{1}{a_4} (\mathbf{T}^{(n)}, \mathbf{T}^{(m)}) - 2a_3 (\mathbf{T}^{(n)} \mathbf{S}, \mathbf{T}^{(m)}) + 2a_2 (\mathbf{T}^{(n)} \mathbf{W}, \mathbf{T}^{(m)}) \right] = (\mathbf{R}, \mathbf{T}^{(m)}) \quad (11)$$

where, for example, the scalar product is defined as  $(\mathbf{T}^{(n)}, \mathbf{T}^{(m)}) = \{\mathbf{T}^{(n)} \mathbf{T}^{(m)}\}$ . In a more compact form,

$$\sum_{n=1}^3 \alpha_n A_{nm} = (\mathbf{R}, \mathbf{T}^{(m)}) \quad (12)$$

where the  $3 \times 3$  matrix  $\mathbf{A}$  is defined as

$$A_{nm} \equiv -(1/a_4) (\mathbf{T}^{(n)}, \mathbf{T}^{(m)}) - 2a_3 (\mathbf{T}^{(n)} \mathbf{S}, \mathbf{T}^{(m)}) + 2a_2 (\mathbf{T}^{(n)} \mathbf{W}, \mathbf{T}^{(m)}) \quad (13)$$

In the two-dimensional mean velocity field case, the matrix  $\mathbf{A}$  is

$$A_{nm} = \begin{bmatrix} -(1/a_4) \eta^2 & -2a_2 \eta^4 \mathcal{R}^2 & -\frac{1}{3} a_3 \eta^4 \\ 2a_2 \eta^4 \mathcal{R}^2 & -(2/a_4) \eta^4 \mathcal{R}^2 & 0 \\ -\frac{1}{3} a_3 \eta^4 & 0 & -(1/6a_4) \eta^4 \end{bmatrix} \quad (14)$$

which, when inverted, leads to the following expressions for the representation coefficients:

$$\alpha_1 = -(a_4/\alpha_0 \eta^2) (\{\mathbf{R}\mathbf{S}\} + 2a_2 a_4 \{\mathbf{R}\mathbf{W}\mathbf{S}\} - 2a_3 a_4 \{\mathbf{R}\mathbf{S}^2\}) \quad (15)$$

$$\alpha_2 = a_4 \left[ a_2 \alpha_1 + \frac{\{\mathbf{R}\mathbf{W}\mathbf{S}\}}{\eta^4 \mathcal{R}^2} \right] \quad (16)$$

$$\alpha_3 = -a_4 \left[ 2a_3 \alpha_1 + \frac{6\{\mathbf{R}\mathbf{S}^2\}}{\eta^4} \right] \quad (17)$$

where  $\alpha_0 = (1 - \frac{2}{3} a_2^2 a_4^2 \eta^2 + 2a_2^2 a_4^2 \eta^2 \mathcal{R}^2)$ . This set of equations is the general solution valid for two-dimensional mean flow and for any arbitrary (symmetric traceless) tensor  $\mathbf{R}$ .

Substituting Eqs. (15–17) into Eq. (9) leads to the representation for the Reynolds stress tensor  $\boldsymbol{\tau}$ :

$$\boldsymbol{\tau} = \frac{2}{3} K \mathbf{I} - 2(-K\alpha_1) \left[ \mathbf{S} + \left( a_2 a_4 + \frac{a_4 \{\mathbf{R}\mathbf{W}\mathbf{S}\}}{\alpha_1 \eta^4 \mathcal{R}^2} \right) (\mathbf{S}\mathbf{W} - \mathbf{W}\mathbf{S}) - \left( 2a_3 a_4 + \frac{6a_4 \{\mathbf{R}\mathbf{S}^2\}}{\alpha_1 \eta^4} \right) \left( \mathbf{S}^2 - \frac{1}{3} \{\mathbf{S}^2\} \mathbf{I} \right) \right] \quad (18)$$

where the  $-K\alpha_1$  term is equivalent to an effective eddy viscosity  $\nu_t^* = C_\mu^* K^2/\varepsilon$ . In most standard  $K-\varepsilon$  models,  $C_\mu^*$  is taken to be a constant value (near 0.09). In contrast, the explicit solution has the effect of yielding a variable  $C_\mu^*$  in the linear component of the stress.

As noted earlier, when a linear pressure-strain correlation model is assumed as well as an isotropic dissipation rate, then  $\mathbf{R} = a_1 \mathbf{S}$ . This expression leads to a right-hand side for Eq. (12) proportional to

$$(\mathbf{R}, \mathbf{T}^{(m)}) = \begin{bmatrix} \{\mathbf{R}\mathbf{S}\} \\ -2\{\mathbf{R}\mathbf{W}\mathbf{S}\} \\ \{\mathbf{R}\mathbf{S}^2\} \end{bmatrix} = \begin{bmatrix} a_1 \eta^2 \\ 0 \\ 0 \end{bmatrix} \quad (19)$$

Thus, in Eqs. (15–18),  $\{\mathbf{R}\mathbf{W}\mathbf{S}\} = \{\mathbf{R}\mathbf{S}^2\} = 0$  in this case.

This result can be related to earlier formulations involving the three-term basis. From Eq. (3), the coefficient  $a_4$  is dependent on  $g$  and as such has a direct dependency on the ratio  $\mathcal{P}/\varepsilon$  from Eq. (4). The solution proposed by Gatski and Speziale<sup>20</sup> for the EASM fixed the value of  $g$ . When  $\mathbf{R} = a_1 \mathbf{S}$ , then

$$\alpha_1 = \frac{-3a_1 a_4}{3 - 2a_2^2 a_4^2 \eta^2 + 6a_2^2 a_4^2 \eta^2 \mathcal{R}^2} \quad (20)$$

In an alternative approach proposed by Ying and Canuto<sup>21</sup> and Girimaji,<sup>22</sup> the value of  $g$  is not fixed; the variation of the production-to-dissipation-rate ratio in the flow is accounted for in the formulation. This approach can also be accounted for in the present formulation. It is easily shown that the production-to-dissipation-rate ratio is given by

$$\mathcal{P}/\varepsilon = -2\{\mathbf{b}\mathbf{S}\}\tau \quad (21)$$

Previously, it has also been shown<sup>23,28</sup> that the invariant  $\{\mathbf{b}\mathbf{S}\}$  is directly related, for two-dimensional flows, to the coefficient  $\alpha_1$  appearing in the tensor representation through

$$\{\mathbf{b}\mathbf{S}\} = \alpha_1 \eta^2 \quad (22)$$

From Eqs. (3) and (4), the coefficient  $a_4$  can then be written as

$$a_4 = [\gamma_1 - 2\gamma_0 \alpha_1 \eta^2 \tau]^{-1} \tau \quad (23)$$

The dependency of  $a_4$  on the production-to-dissipation-rate ratio through  $\alpha_1$  makes both sides of Eq. (15) functions of  $\alpha_1$ . This dependency results in a cubic equation for  $\alpha_1$  given by

$$\gamma_0^2 \alpha_1^3 - \frac{\gamma_0 \gamma_1}{\eta^2 \tau} \alpha_1^2 + \frac{1}{4\eta^4 \tau^2} \left[ \gamma_1^2 - 2\tau^2 \gamma_0 \{\mathbf{R}\mathbf{S}\} - 2\eta^2 \tau^2 \left( \frac{a_2^2}{3} - \mathcal{R}^2 a_2^2 \right) \right] \alpha_1 + \frac{1}{4\eta^6 \tau} [\gamma_1 \{\mathbf{R}\mathbf{S}\} + 2\tau (a_2 \{\mathbf{R}\mathbf{W}\mathbf{S}\} - a_3 \{\mathbf{R}\mathbf{S}^2\})] = 0 \quad (24)$$

Even with this more complicated expression for  $\alpha_1$ , the expansion coefficients of the nonlinear terms  $\alpha_2$  and  $\alpha_3$  retain the same functional dependency on  $\alpha_1$  as before. When expressed in terms of the production-to-dissipation-rate ratio with  $\mathbf{R} = a_1 \mathbf{S}$ , Eq. (24) can be shown<sup>23</sup> to be equivalent to earlier results.<sup>21,22</sup>

Recent results<sup>21,31</sup> as well as the results from this study have shown that robustness characteristics and predictive performance are improved when the variation of the production-to-dissipation-rate ratio is allowed. Thus Eq. (24) (with  $\mathbf{R} = a_1 \mathbf{S}$ ) is currently solved for  $\alpha_1$ . Previously,<sup>21,22</sup> the selection of the proper root for the solution

of Eq. (24) was done on the basis of continuity arguments. Here the proper choice for the solution root is based on the asymptotic analysis of Jongen and Gatski.<sup>24</sup> It was found that the root with the lowest real part leads to the correct choice for  $\alpha_1$ . The remaining expansion coefficients  $\alpha_2$  and  $\alpha_3$  are then extracted from Eqs. (16) and (17).

The explicit tensor representation given in Eq. (18) is coupled with a  $K$ - $\varepsilon$  two-equation model. The transport equations for the turbulent kinetic energy  $K$  and dissipation rate  $\varepsilon$  are

$$\frac{DK}{Dt} = \mathcal{P} - \varepsilon + \frac{\partial}{\partial x_k} \left[ \left( \nu + \frac{\nu_t}{\sigma_K} \right) \frac{\partial K}{\partial x_k} \right] \quad (25)$$

$$\frac{D\varepsilon}{Dt} = C_{\varepsilon 1} \frac{\varepsilon}{K} \mathcal{P} - f_{\varepsilon} C_{\varepsilon 2} \frac{\varepsilon^2}{K} + \frac{\partial}{\partial x_k} \left[ \left( \nu + \frac{\nu_t}{\sigma_{\varepsilon}} \right) \frac{\partial \varepsilon}{\partial x_k} \right] \quad (26)$$

where  $\nu$  is the kinematic viscosity,  $\nu_t = C_{\mu} K \tau$  is an equilibrium turbulent eddy viscosity, and

$$\mathcal{P} = -\tau_{ij} \frac{\partial u_i}{\partial x_j} = -2(bS)K \quad (27)$$

$$f_{\varepsilon} = [1 - \exp(-Re_K/10.8)], \quad Re_K = (K^{1/2} d / \nu) \quad (28)$$

$$\sigma_K = 1.0, \quad \sigma_{\varepsilon} = [\kappa^2 / \sqrt{C_{\mu}} (C_{\varepsilon 2} - C_{\varepsilon 1})]$$

$$\kappa = 0.41, \quad C_{\varepsilon 1} = 1.44, \quad C_{\varepsilon 2} = 1.83, \quad C_{\mu} = 0.096 \quad (29)$$

and  $d$  is the distance to the nearest wall. Additional wall damping functions (such as  $f_{\mu}$ , to achieve expected asymptotic behavior of the turbulence quantities very near the wall) are not employed in the current model. This avoids the need for further calibration constants and has no noticeable effect on  $c_f$  or any turbulent or mean flow prediction in and above the log layer.

#### IV. Results

The U-duct configuration is shown in Fig. 1. The turn has an inner radius of  $r_i = 1.91$  cm and an outer radius of  $r_o = 5.72$  cm. The finest grid employed is  $417 \times 153$  and extends from  $x/H = -4$  upstream of the bend to  $x/H = 13.12$  downstream. The minimum normal spacing at the walls is  $1.0 \times 10^{-5}$  cm, which yields an average  $y^+$  value of less than 0.2. Coarser grids, used to investigate grid sensitivity, are formed from the fine grid by successively eliminating every other grid point. (The grid shown in Fig. 1 is a part of the medium-level  $209 \times 77$  grid.) The nominal Mach number for this flow is  $M = 0.1$ , and the Reynolds number based on channel width  $H$  is  $10^6$ .

At the upstream boundary, the  $u$ -velocity profile is set based on the experimentally measured skin friction and boundary-layer thickness. The  $K$  and  $\varepsilon$  values are specified in a way similar to that used by Monson et al.,<sup>5</sup> as follows. In the near-wall region ( $y^+ < 4$ ), the values for  $K$  are obtained from the expression  $K^+ = 0.05(y^+)^2$ . The peak  $K$  is specified to match experiment and is assumed to be at  $y^+ = 20$ . The value of  $\varepsilon$  is computed from  $\varepsilon = C_{\mu}^{3/4} K^{3/2} / L_m$ , with

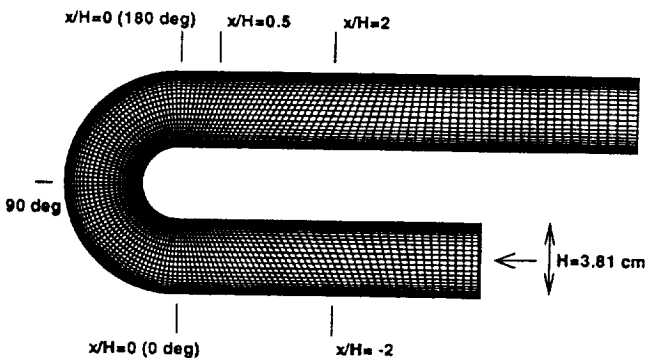


Fig. 1 U-duct configuration (portion of  $209 \times 77$  grid shown).

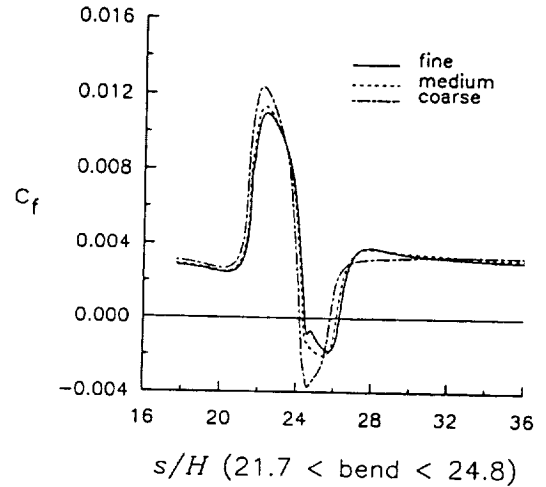


Fig. 2 Effect of grid density on inner surface skin friction using EASM.

$L_m = \kappa y$  in the inner region and  $L_m = 0.09\delta$  in the outer region. Also at the upstream boundary, the density is specified at  $\rho/\rho_{ref} = 1$ , and the pressure is extrapolated from the interior of the grid. At the outflow boundary, pressure is specified at  $p/p_{ref} = 1$ , and all other quantities are extrapolated from the interior of the grid.

#### A. Grid Sensitivity Study

Figure 2 shows the inner wall skin-friction coefficient using the EASM turbulence model on three grids. The  $s$  in Fig. 2 indicates the distance of the channel centerline from a reference point approximately 83 cm upstream of the start of the bend. Except in the separated flow region, there is very little difference between the medium and fine grid results. The coarse grid ( $105 \times 39$ ) yields significant differences from the two finer grids even outside of the separated region. Results using other turbulence models show generally similar or smaller grid sensitivities. Although not shown, mean flow and turbulence quantities upstream of separation indicate grid-converged levels even for the medium grid.

For the remainder of the study, all results (with one exception) were obtained using the fine grid only. On the basis of the results of this grid sensitivity study, we are confident that even the medium grid level is fine enough to capture the essential physics of this case, particularly upstream of the separated region (which is our primary focus in this study). Use of the fine grid adds an additional level of confidence that any differences between computations and experiment are due to the modeled physics and not due to numerical discretization errors.

#### B. Results Using Three Turbulence Models

The three turbulence models used in this study represent three successive levels of representation in describing the development and evolution of the turbulence. The EASM represents the highest level; it is derived directly from the RSM as described earlier and is implemented in a two-equation  $K$ - $\varepsilon$  formulation. The SST model is a two-equation linear eddy viscosity model, and the S-A model is a one-equation linear eddy viscosity model. (The RSM, results of which are discussed in a separate subsection, utilizes seven equations to solve for the turbulence. Its results are not included in this section because the RSM is generally too expensive. Therefore, it is not considered to be a viable model at the present time for general use with complex configurations.)

Although not shown, all three turbulence models do an excellent job predicting the flow upstream of the turn. At the start of the bend, at  $x/H = 0$  (0 deg), however, computed Reynolds shear stresses are already showing significant differences from the experimentally measured levels (Fig. 3) near the inner wall. In Fig. 3,  $u_{ref}$  is the velocity corresponding to  $M_{ref} = 0.1$ , and  $dist = 0$  at the inner wall. Although not shown, all models at this  $x/H = 0$  (0 deg) station still predict the mean streamwise velocity in good agreement with each other and with experiment.

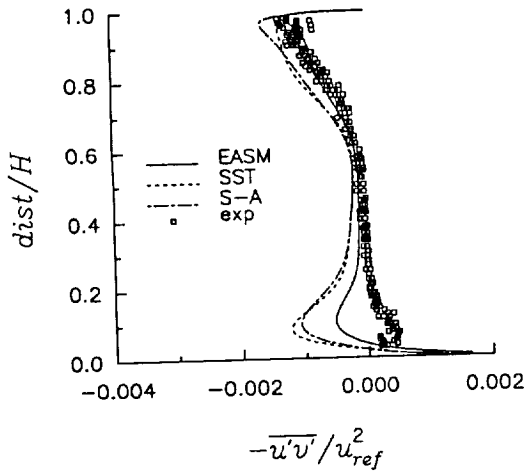


Fig. 3 Reynolds shear stress at 0 deg in the bend.

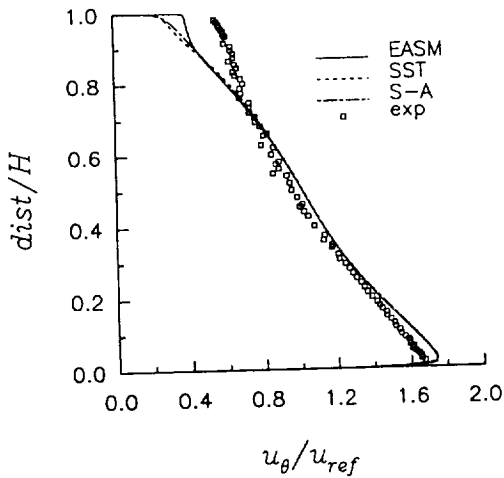


Fig. 4 Streamwise velocity at 90 deg in the bend.

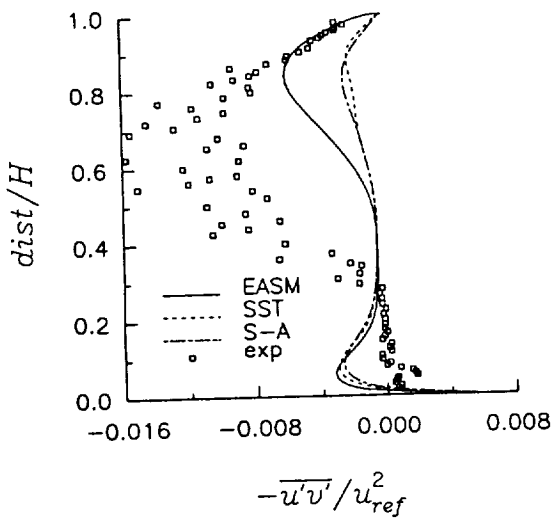


Fig. 5 Reynolds shear stress at 90 deg in the bend.

Figures 4 and 5 show mean streamwise velocity and Reynolds shear stress, respectively, at the 90-deg position halfway around the bend. All models predict similar velocity profiles (Fig. 4). Overall, these results are in reasonable agreement with experiment, although the velocity magnitude near the inner wall is slightly over-predicted and the velocity magnitude near the outer wall is under-predicted. In Fig. 5, the results for the three turbulence models are very similar near the convex wall: None of the models

predict near-zero levels of Reynolds shear stress, as seen in the experiment.

In the outer half of the channel, all models underpredict the magnitude of  $\overline{u'v'}$ . This behavior was also seen by Luo and Lakshminarayana.<sup>12</sup> Some researchers have found that three-dimensional Taylor-Gortler (streamwise) vortices may exist near concave walls, but their existence is disputed.<sup>3</sup> Nonetheless, spanwise variations are often seen, bringing into question the suitability of two-dimensional computations for predicting quantities near a concave wall. For this reason, in the remainder of the paper we focus only on the behavior of the turbulence models near the inner (convex) wall. The suppressive effect of convex curvature on Reynolds shear stress is well known, and it is believed that the Monson and Seegmiller<sup>4</sup> experiment suffices as a suitable testbed for investigating two-dimensional turbulence model behavior in that region.

Pressure and skin-friction coefficients along the inner wall are shown in Figs. 6 and 7. All three turbulence models predict the separation location somewhat too far downstream in comparison with experiment, but predict comparable separation lengths in good agreement with the data. Overall, the EASM predicts the pressure levels downstream of the bend in slightly better agreement with experiment than the predictions of the other models. Although not shown, note that all three of the turbulence models exhibit a too-slow recovery from separation. This trend was also seen in Ref. 12 and is a well-recognized feature of most turbulence models in use today.<sup>32</sup>

C. EASM Analysis

The EASM used in this study accounts for the variation of the production-to-dissipation-rate ratio; that is,  $g$  [Eq. (4)] is variable.

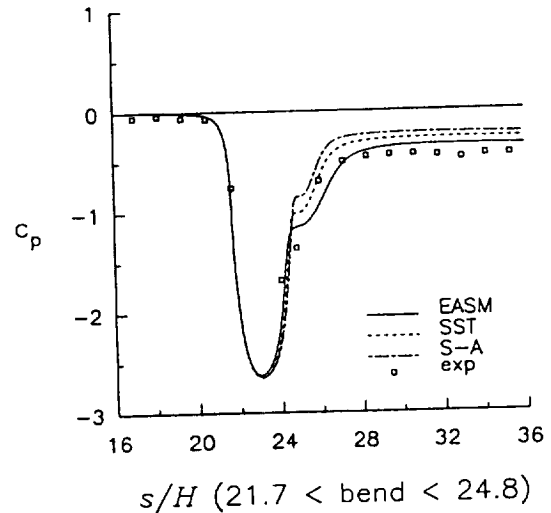


Fig. 6 Inner-surface pressure coefficient.

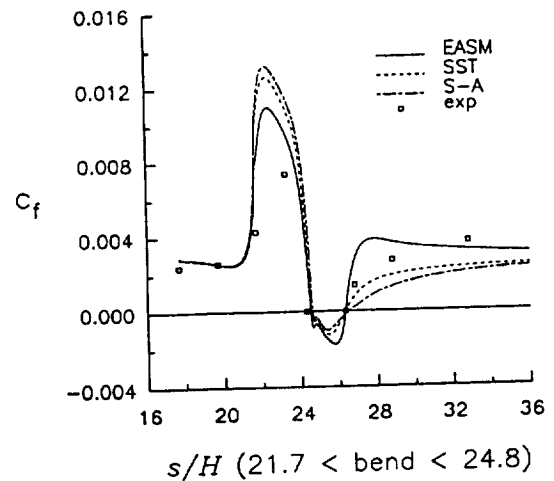


Fig. 7 Inner-surface skin-friction coefficient.

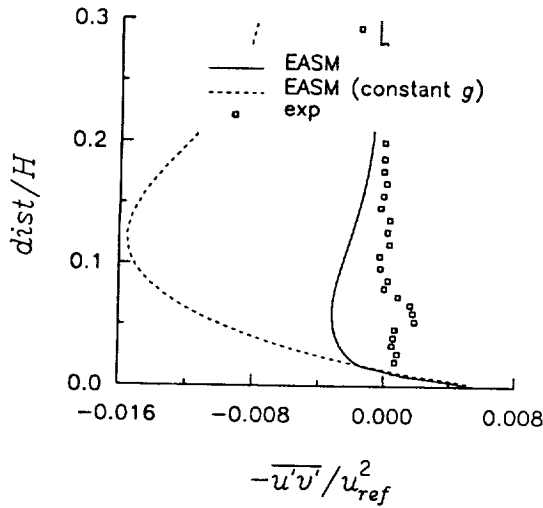


Fig. 8 Effect of constant  $g = 0.233$  (Ref. 20) in EASM on the Reynolds shear stress near the inner wall at 90 deg in the bend.

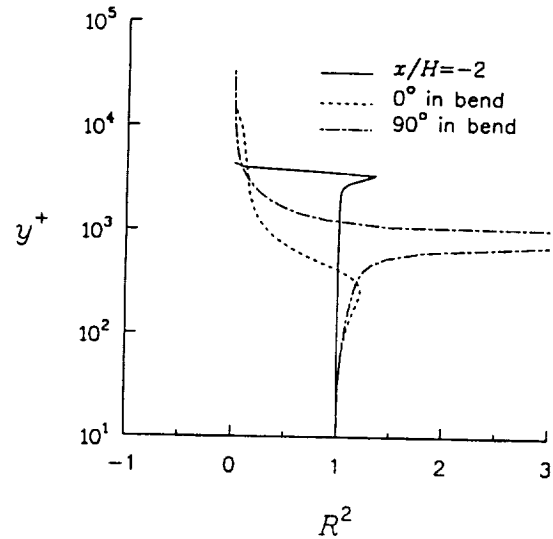


Fig. 10  $R^2$  levels near the inner wall computed at three stations.

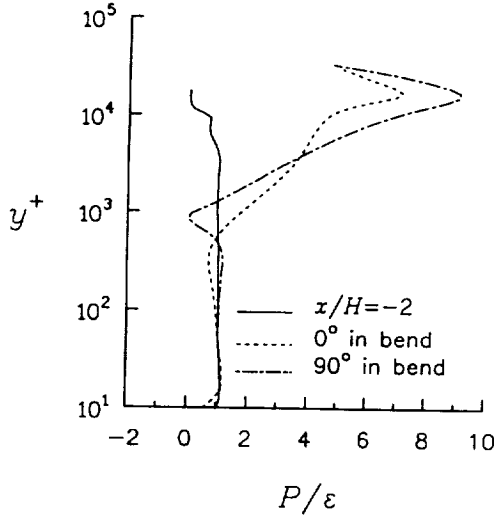


Fig. 9 Production-to-dissipation-rate ratio near the inner wall computed at three stations.

As will be shown, if  $g$  is held constant<sup>20</sup> at 0.233 (corresponding to the equilibrium value of  $P/\epsilon = 1.886$  for homogeneous shear flow), predictions of turbulence quantities in the curvature region of this flowfield are poor.

For example, computed Reynolds shear stresses at 90 deg in the bend using EASM with constant  $g = 0.233$  are shown in Fig. 8 in comparison with results from the variable  $g$  model. The constant  $g$  model dramatically overpredicts the magnitudes of  $\overline{u'v'}$  near the inner wall in this region. ( $K$ , not shown, is also significantly over-predicted.) The constant  $g$  model also yields a significantly smaller region of separation in comparison with the other models.<sup>33</sup>

As shown in Fig. 9, the computed value of  $P/\epsilon$  is far from 1 (which is the equilibrium value in the log layer of a channel flow) over much of the channel outside of the inner-wall log layer at the stations where curvature is present. Figure 10 is a plot of the flow parameter  $R^2$  as a function of  $y^+$  at the same three locations shown in Fig. 9. At the  $x/H = -2$  station well upstream of the bend,  $R^2 \approx 1$  (except in the middle of the channel), representing pure shear flow, as expected. Also,  $R^2 \approx 1$  within the lower part of the log layers at all three stations. However,  $R^2$  deviates significantly from 1 for the flow outside  $y^+ \approx 500$  at the two stations in the bend. At both locations,  $R^2$  approaches 0 at large  $y^+$ , representing plane strain flow.

As discussed by Rumsey et al.,<sup>33</sup> EASM with variable  $g$  and EASM with constant  $g$  behave quite differently when  $P/\epsilon$  is far from 1–2. In particular, when  $R^2$  is near zero and  $P/\epsilon > 2$ , the constant  $g$  model yields smaller values of  $\eta\tau$  for a given value of  $P/\epsilon$ . Because  $\alpha_1$  is proportional to  $-(P/\epsilon)/\eta^2$  [from Eqs. (21) and

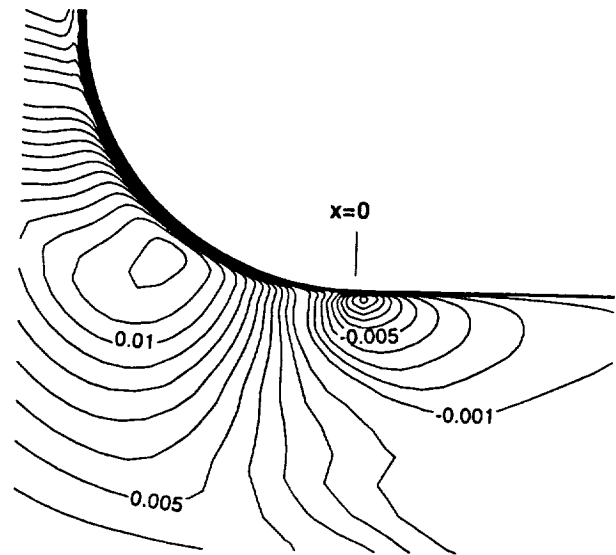


Fig. 11 Contour plot of  $Db_{11}/Dt$  in the vicinity of the start of curvature using RSM (flow is from right to left).

(22)], the EASM with constant  $g$  predicts significantly larger levels of  $v_i^*$  outside the log layer in the curved region of the flow than EASM with variable  $g$ . This is the source of the larger predicted  $\overline{u'v'}$  peak for EASM (constant  $g$ ) in Fig. 8.

#### D. Comparison with RSM

Next, the U-duct flow is solved with an RSM using the ISAAC code on the  $209 \times 77$  grid. Our focus is not to compare global results, but rather to explore in detail the behavior near convex curvature. As will be shown, the RSM is in better agreement with experiment at both  $x = 0$  and at 90 deg in the bend than the three models used thus far. These results are also consistent with Ref. 12.

Evidently, one or more of the assumptions that go into the derivation of the EASM is causing the model to deviate from the RSM result for this flow in the curved (bend) region. Recall that two of the primary assumptions in developing the algebraic relationship are given in Eqs. (5) and (6). Therefore, we scrutinize the computed levels of each of these terms from the RSM solution. Figure 11 shows contours of  $Db_{11}/Dt$  (nondimensionalized by  $L/a_\infty$ ) near the start of the bend. Other  $Db_{ij}/Dt$  terms are of similar magnitude. Near  $x = 0$  (0 deg in the bend),  $Db_{11}/Dt$  is negative (at a maximum level of about  $-0.01$ ), followed by a positive peak at a maximum of approximately 0.012 somewhat downstream. These levels of  $Db_{11}/Dt$  are of the same order of magnitude as the nondimensional  $a_1 S_{11}$  levels at the same locations (not shown), which indicates that the first term in

Eq. (1) ( $=D\mathbf{b}/Dt$ ) is important in this region of the flow and should not be neglected. The  $\mathcal{D}_{ij} - (\tau_{ij}/2K)\mathcal{D}_{nn}$  terms computed from the RSM solution are very small in comparison with the  $D\mathbf{b}/Dt$  terms, of order  $10^{-8}$ . Therefore, it is not expected that neglecting them in the derivation of the EASM has any impact for this flowfield.

The deficiency in imposing the equilibrium condition  $D\mathbf{b}/Dt = 0$  in the development of the EASM is apparent. In a strongly curved flow, such as the U-duct, the equilibrium condition needs to be relaxed. In the context of the algebraic stress formulation, it has recently been shown<sup>34</sup> that imposing the equilibrium assumption on the anisotropy  $\mathbf{b}$  in a locally varying noninertial coordinate frame throughout the flow accounts for the extrastrain effects introduced by the curvature. This new (local) frame is simply the principal axes of the strain rate tensor whose rotation is a measure of curvature effects on the flow. The equilibrium condition imposed in the noninertial frame can then be recast in the inertial frame as an inhomogeneous condition on  $D\mathbf{b}/Dt$ . Spalart and Shur<sup>35</sup> also used the principal axes frame of reference to account for system rotation and curvature in sensitizing the S-A model.

Under a Euclidean transformation,<sup>36</sup> the turbulence anisotropy tensor  $b_p^q$  transformation from a Cartesian base system is simply given by

$$\bar{b}_i^j = X_i^p b_p^q \bar{X}_q^j \quad (30)$$

where  $\bar{X}_q^j(t)$  is the proper orthogonal tensor (and  $X_i^p$  is its transpose) that represents the transformation to the local principal axes frame. It then follows that the material derivative of Eq. (30) yields

$$\frac{D\bar{b}_i^j}{Dt} = X_i^p \frac{Db_p^q}{Dt} \bar{X}_q^j + \frac{D}{Dt} [X_i^p] b_p^q \bar{X}_q^j + X_i^p b_p^q \frac{D}{Dt} [\bar{X}_q^j] \quad (31)$$

If the equilibrium assumption is now applied to the transformed frame, so that  $D\bar{b}/D\bar{t} = 0$ , then Eq. (31) can be rewritten as

$$\frac{Db_p^q}{Dt} = b_p^k \Omega_k^q - \Omega_p^k b_k^q, \quad \Omega_p^q = \bar{X}_p^k \frac{D}{Dt} [X_k^q] \quad (32)$$

or, in matrix notation

$$\frac{D\mathbf{b}}{Dt} = \mathbf{b}\mathbf{\Omega} - \mathbf{\Omega}\mathbf{b}, \quad \mathbf{\Omega} = \bar{\mathbf{X}} \frac{D}{Dt} [\mathbf{X}] \quad (33)$$

Equation (33) is the (inhomogeneous) condition to be applied to  $D\mathbf{b}/Dt$  in the inertial frame instead of the equilibrium condition  $D\mathbf{b}/Dt = 0$ . Equation (7) then becomes

$$-(1/a_4)\mathbf{b} - a_3(\mathbf{b}\mathbf{S} + \mathbf{S}\mathbf{b} - \frac{2}{3}(\mathbf{b}\mathbf{S})\mathbf{I}) + a_2(\mathbf{b}\bar{\mathbf{W}} - \bar{\mathbf{W}}\mathbf{b}) = \mathbf{R} \quad (34)$$

where the absolute rotation rate tensor  $\bar{\mathbf{W}}$  is given by

$$\bar{\mathbf{W}} = (1/a_2)\mathbf{\Omega} \quad (35)$$

Thus, the only change to the explicit algebraic model formulation is to replace the rotation rate tensor  $\mathbf{W}$  with the absolute rotation rate tensor  $\bar{\mathbf{W}}$ . A similar formulation to this was described by Girimaji<sup>37</sup>; however, he used the unit vector in the direction of acceleration rather than the principal strain direction to define the noninertial frame.

With this new assumption in the EASM, results at 0 and 90 deg in the bend shown in Figs. 12 and 13 now show improved predictions of  $\overline{u'v'}$  near the inner wall, in better agreement with both RSM and experiment. The main effect of the better-predicted Reynolds shear stresses is a lower skin friction in the curved region and a small lengthening of the separated region compared to the baseline EASM result. Aside from this change, there are only relatively minor effects of the curvature correction on mean-flow parameters for this case. This behavior differs from that exhibited by the S-A model with curvature correction for this same case in Ref. 38. Shur et al.<sup>38</sup> showed that the inclusion of their correction term has a dramatic effect on the separation location and extent as well as on the surface pressures downstream, compared to the baseline model. Most notably, the modified model significantly overpredicts the sep-

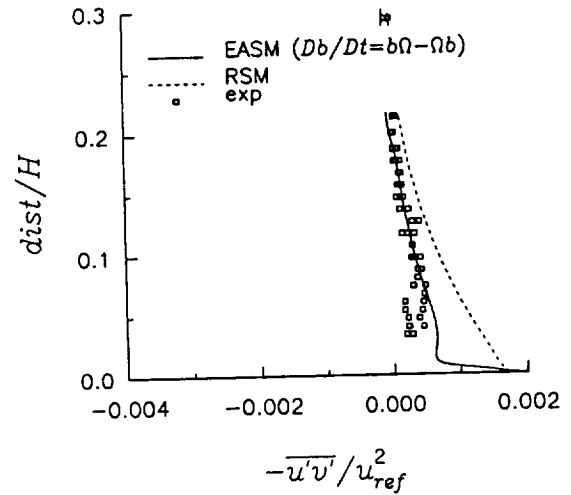


Fig. 12 Reynolds shear stress near the inner wall at 0 deg in the bend.

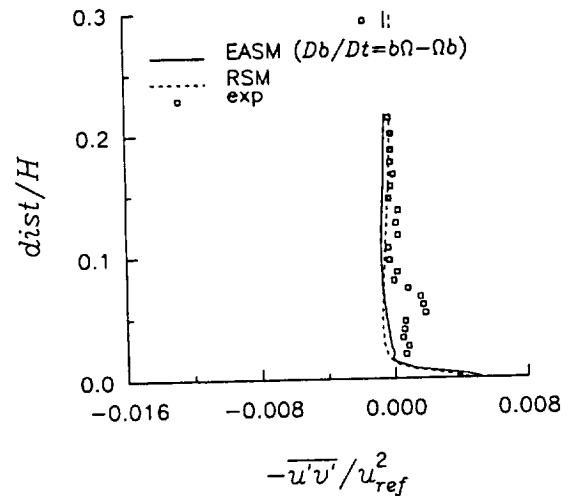


Fig. 13 Reynolds shear stress near the inner wall at 90 deg in the bend.

aration length. Shur et al. believed this overprediction was due to possible deficiencies in the original S-A model itself, and not to the curvature correction. Note, however, that the S-A curvature correction, although based similarly on the rate of change of the principal axes, includes a heuristic rotation function that multiplies the model's production term. This implementation method is quite different from the current EASM implementation, which includes the effect of curvature into Eq. (18) primarily through the  $\alpha_1$  term, which is modified by using  $\bar{\mathbf{W}}$  in place of  $\mathbf{W}$  in Eq. (24) [ $\bar{\mathbf{W}}$  is also used in the nonlinear term in Eq. (18), but this has a secondary effect in this case].

An additional test case was run (using only EASM) as a further validation of the EASM curvature correction. The duct configuration of Smits et al.<sup>25</sup> is shown in Fig. 14. The flow undergoes a strong curvature ( $\delta/R \approx 0.17$ ) of short duration. The duct turns through 30 deg with a radius of curvature on the inner wall of 127 mm. Nominal Mach number in the duct is 0.097 and Reynolds number based on  $H$  is taken to be  $3 \times 10^5$ . We again focus on results near the convex wall. Figure 15 shows Reynolds shear stress downstream of the bend at  $x = 30$  mm (where  $\delta \approx 21$  mm). The curvature-corrected model captures the suppression of the Reynolds shear stress in the upper part of the boundary layer, whereas the original EASM does not. Like the U-duct case, in spite of the change in Reynolds shear stress, the effect of the curvature correction on mean-flow parameters is again relatively small. Figure 16 shows velocity profiles at three stations downstream of the bend. There is almost no difference between EASM with and without the curvature correction, and the character of the experimental data is well predicted.

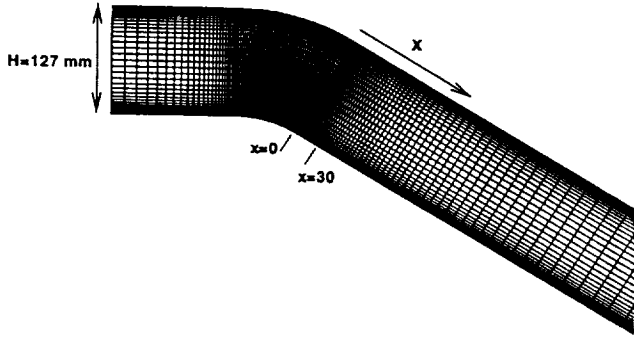


Fig. 14 Curved (30-deg) duct configuration (portion of  $161 \times 81$  grid shown).

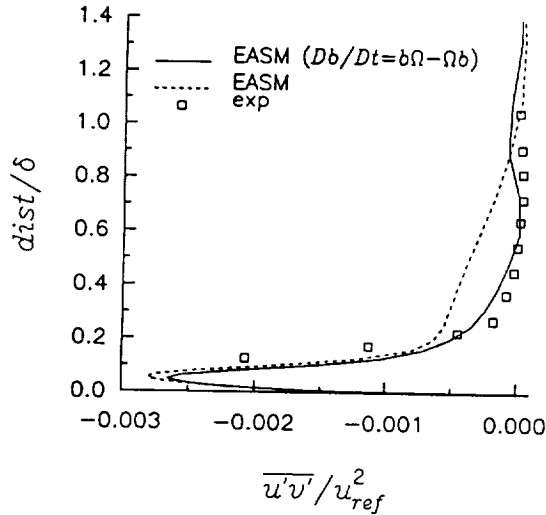


Fig. 15 Reynolds shear stress at  $x = 30$  mm in 30-deg curved duct.

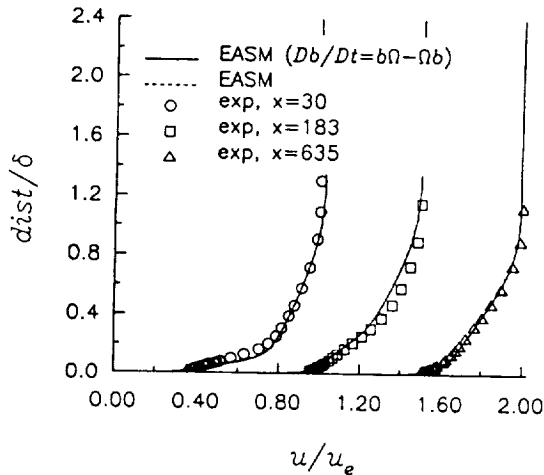


Fig. 16 Velocity profiles in 30-deg curved duct. (Each successive station is offset by 0.5 units to the right.)

## V. Conclusions

The ability of three types of turbulence models to predict two-dimensional curvature effects was investigated for a model test problem. It was shown that an EASM performs better than one- or two-equation eddy viscosity models, provided that the variation of the production-to-dissipation-rate ratio in the flow is accounted for in the EASM formulation. Theoretical analysis of the EASM provided some insight into the differences in the behavior of this model in the curved region of the flow when  $g$  is held constant.

In their original formulations, none of the one- or two-equation turbulence models used in this study captured the full extent of suppressed turbulence near the convex wall. However, a full Reynolds

stress turbulence model did. Some of the assumptions that go into the derivation of the EASM were investigated and compared with the computed flowfield from the full RSM. Through this analysis, the algebraic model assumption that  $Db_{ij}/Dt = 0$  was found to be the source of error in the strong curvature region. By accounting for the local variation of the principal axes of the strain rate tensor, the EASM correctly predicted the suppressed turbulence in the outer part of the boundary layer near the convex wall.

## References

- Lynch, F. T., Potter, R. C., and Spaid, F. W., "Requirements for Effective High-Lift CFD," *International Council of the Aeronautical Sciences (ICAS) Proceedings, 20th Congress*, Vol. 2, AIAA, Reston, VA, 1996, pp. 1479-1492.
- Ying, S. X., Spaid, F. W., McGinley, C. B., and Rumsey, C. L., "Investigation of Confluent Boundary Layers in High-Lift Flow," *Journal of Aircraft*, Vol. 36, No. 3, 1999, pp. 550-562.
- Patel, V. C., and Sotiropoulos, F., "Longitudinal Curvature Effects in Turbulent Boundary Layers," *Progress in Aerospace Sciences*, Vol. 33, 1997, pp. 1-70.
- Monson, D. J., and Seegmiller, H. L., "An Experimental Investigation of Subsonic Flow in a Two-Dimensional U-Duct," NASA TM 103931, July 1992.
- Monson, D. J., Seegmiller, H. L., McConaughy, P. K., and Chen, Y. S., "Comparison of Experiment with Calculations Using Curvature-Corrected Zero and Two-Equation Turbulence Models for a Two-Dimensional U-Duct," AIAA Paper 90-1484, June 1990.
- Sandborn, V. A., and Marcy, S. J., "Evaluation of High Reynolds Number Flow in a 180 Degree Turn-Around-Duct," NASA CR 184243, 1991.
- So, R. M. C., and Mellor, G. L., "Experiment on Convex Curvature Effects in Turbulent Boundary Layers," *Journal of Fluid Mechanics*, Vol. 60, Pt. 1, 1973, pp. 43-62.
- Gillis, J. C., and Johnston, J. P., "Turbulent Boundary-Layer Flow and Structure on a Convex Wall and its Redevelopment on a Flat Wall," *Journal of Fluid Mechanics*, Vol. 135, 1983, pp. 123-153.
- Kim, W. J., and Patel, V. C., "An Experimental Study of Boundary-Layer Flow in a Curved Rectangular Duct," *ASME Fluids Engineering Conference*, FED-Vol. 146, American Society of Mechanical Engineers, New York, 1993, pp. 13-28.
- Launder, B. E., and Loizou, P. A., "Laminarization of Three-Dimensional Accelerating Boundary Layers in a Curved Rectangular-Sectioned Duct," *International Journal of Heat and Fluid Flow*, Vol. 13, No. 2, 1992, pp. 124-131.
- Schwarz, A. C., and Plesniak, M. W., "Convex Turbulent Boundary Layers with Zero and Favorable Pressure Gradients," *Journal of Fluids Engineering*, Vol. 118, Dec. 1996, pp. 787-794.
- Luo, J., and Lakshminarayana, B., "Prediction of Strongly Curved Turbulent Duct Flows with Reynolds Stress Model," *AIAA Journal*, Vol. 35, No. 1, 1997, pp. 91-98.
- Rodi, W., and Scheuerer, G., "Calculation of Curved Shear Layers with Two-Equation Turbulence Models," *Physics of Fluids*, Vol. 26, No. 6, 1983, pp. 1422-1436.
- Luo, J., and Lakshminarayana, B., "Analysis of Streamline Curvature Effects on Wall-Bounded Turbulent Flows," *AIAA Journal*, Vol. 35, No. 8, 1997, pp. 1273-1279.
- Iacovides, H., Launder, B. E., Loizou, P. A., and Zhao, H. H., "Turbulent Boundary-Layer Development Around a Square-Sectioned U-Bend: Measurements and Computation," *Journal of Fluids Engineering*, Vol. 112, Dec. 1990, pp. 409-415.
- Shima, N., "Prediction of Turbulent Boundary Layers with a Second-Moment Closure: Part II—Effects of Streamline Curvature and Spanwise Rotation," *Journal of Fluids Engineering*, Vol. 115, March 1993, pp. 64-69.
- Rumsey, C. L., Gatski, T. B., Ying, S. X., and Bertelrud, A., "Prediction of High-Lift Flows Using Turbulent Closure Models," *AIAA Journal*, Vol. 36, No. 5, 1998, pp. 765-774.
- Spalart, P. R., and Allmaras, S. R., "A One-Equation Turbulence Model for Aerodynamic Flows," *La Recherche Aeronautique*, No. 1, 1994, pp. 5-21.
- Menter, F. R., "Improved Two-Equation  $k-\omega$  Turbulence Models for Aerodynamic Flows," NASA TM 103975, Oct. 1992.
- Gatski, T. B., and Speziale, C. G., "On Explicit Algebraic Stress Models for Complex Turbulent Flows," *Journal of Fluid Mechanics*, Vol. 254, 1993, pp. 59-78.
- Ying, R., and Canuto, V. M., "Turbulence Modelling over Two-Dimensional Hills Using an Algebraic Reynolds Stress Expression," *Boundary-Layer Meteorology*, Vol. 77, 1996, pp. 69-99.
- Girimaji, S. S., "Fully Explicit and Self-Consistent Algebraic Reynolds Stress Model," *Theoretical and Computational Fluid Dynamics*, Vol. 8, 1996, pp. 387-402.

- <sup>23</sup>Jongen, T., and Gatski, T. B., "A New Approach to Characterizing the Equilibrium States of the Reynolds Stress Anisotropy in Homogeneous Turbulence," *Theoretical and Computational Fluid Dynamics*, Vol. 11, 1998, pp. 31-47; Erratum: *Theoretical and Computational Fluid Dynamics*, Vol. 12, 1998, pp. 71, 72.
- <sup>24</sup>Jongen, T., and Gatski, T. B., "A Unified Analysis of Planar Homogeneous Turbulence Using Single-Point Closure Equations," *Journal of Fluid Mechanics*, Vol. 399, 1999, pp. 117-150.
- <sup>25</sup>Smits, A. J., Young, S. T. B., and Bradshaw, P., "The Effect of Short Regions of High Surface Curvature on Turbulent Boundary Layers," *Journal of Fluid Mechanics*, Vol. 94, Pt. 2, 1979, pp. 209-242.
- <sup>26</sup>Krist, S. L., Biedron, R. T., and Rumsey, C. L., "CFL3D User's Manual (Version 5.0)," NASA TM-1998-208444, June 1998.
- <sup>27</sup>Morrison, J. H., "A Compressible Navier-Stokes Solver with Two-Equation and Reynolds Stress Turbulence Closure Models," NASA CR-4440, May 1992.
- <sup>28</sup>Jongen, T., and Gatski, T. B., "General Explicit Algebraic Stress Relations and Best Approximation for Three-Dimensional Flows," *International Journal of Engineering Science*, Vol. 36, 1998, pp. 739-763.
- <sup>29</sup>Speziale, C. G., Sarkar, S., and Gatski, T. B., "Modeling the Pressure-Strain Correlation of Turbulence: An Invariant Dynamical Systems Approach," *Journal of Fluid Mechanics*, Vol. 227, 1991, pp. 245-272.
- <sup>30</sup>Astarita, G., "Objective and Generally Applicable Criteria for Flow Classification," *Journal of Non-Newtonian Fluid Mechanics*, Vol. 6, 1979, pp. 69-76.
- <sup>31</sup>Jongen, T., Machiels, L., and Gatski, T. B., "Predicting Noninertial Effects with Linear and Nonlinear Eddy-Viscosity and Algebraic Stress Models," *Flow, Turbulence, and Combustion*, Vol. 60, 1998, pp. 215-234.
- <sup>32</sup>Johnson, D. A., Menter, F. R., and Rumsey, C. L., "Status of Turbulence Modeling for External Aerodynamics," AIAA Paper 94-2226, June 1994.
- <sup>33</sup>Rumsey, C. L., Gatski, T. B., and Morrison, J. H., "Turbulence Model Predictions of Extra-Strain Rate Effects in Strongly Curved Flows," AIAA Paper 99-0157, Jan. 1999.
- <sup>34</sup>Gatski, T. B., and Rumsey, C. L., "Linear and Non-Linear Eddy Viscosity Models," *Closure Strategies for Turbulent and Transitional Flows*, edited by B. E. Launder and N. D. Sandham, Cambridge Univ. Press, Cambridge, England, U.K. (to be published).
- <sup>35</sup>Spalart, P. R., and Shur, M., "On the Sensitization of Turbulence Models to Rotation and Curvature," *Aerospace Science and Technology*, No. 5, 1997, pp. 297-302.
- <sup>36</sup>Speziale, C. G., "Invariance of Turbulent Closure Models," *Physics of Fluids*, Vol. 22, No. 6, 1979, pp. 1033-1037.
- <sup>37</sup>Girimaji, S. S., "A Galilean Invariant Explicit Algebraic Reynolds Stress Model for Turbulent Curved Flows," *Physics of Fluids*, Vol. 9, No. 4, 1997, pp. 1067-1077.
- <sup>38</sup>Shur, M., Strelets, M., Travin, A., and Spalart, P. R., "Turbulence Modeling in Rotating and Curved Channels: Assessment of the Spalart-Shur Correction Term," AIAA Paper 98-0325, Jan. 1998.

R. M. C. So  
Associate Editor

